International Journal of Nanomedicine

Dovepress
open access to scientific and medical research

Open Access Full Text Article

ORIGINAL RESEARCH

Engineered Polymeric Nanovector for Intracellular Peptide Delivery in Antitumor Therapy

Xi Zhang[1,*], Mingming Zhang[1,*], Sijun Huang[1], Kiyoshi Ohtani[2], Li Xu[1], Yi Guo[1]

[1]Key Laboratory for Molecular Enzymology and Engineering, the Ministry of Education, National Engineering Laboratory for AIDS Vaccine, School of Life Sciences, Jilin University, Changchun, 130012, People's Republic of China; [2]Department of Biomedical Sciences, School of Biological and Environmental Sciences, Kwansei Gakuin University, Sanda, Hyogo, 669-1337, Japan

*These authors contributed equally to this work

Correspondence: Li Xu; Yi Guo, Key Laboratory for Molecular Enzymology and Engineering, the Ministry of Education, National Engineering Laboratory for AIDS Vaccine, School of Life Sciences, Jilin University, Changchun, 130012, People's Republic of China, Email xuli@jlu.edu.cn; guoyi@jlu.edu.cn

Objective: This study aimed to deliver a polypeptide from the Bax-BH3 domain (BHP) through the synthesis of self-assembled amphiphile nanovectors (NVs) and to assess their potential for cancer therapeutic applications and biological safety in vitro and in vivo. These findings provide valuable options for cancer intervention and a novel approach for the rational design of therapeutics.

Methods: We studied the antitumor activity of BHP by preparing RGDfK-PHPMA-b-Poly (MMA-*alt*-(Rhob-MA)) (RPPMMRA) and encapsulating it in BHP-NV. We also performed a series of characterizations and property analyses of RPPMMRA, including its size, stability, and drug-carrying capacity. The biocompatibility of RPPMMRA was evaluated in terms of cytotoxicity and hemolytic effects. The pro-apoptotic capacity of BHP was evaluated in vitro using mitochondrial membrane potential, flow cytometry, and apoptosis visualization techniques. The potential therapeutic effects of BHP on tumors were explored using reverse molecular docking. We also investigated the in vivo proapoptotic effect of BHP-NV in a nude mouse tumor model.

Results: NVs were successfully prepared with hydrated particle sizes ranging from 189.6 nm to 256.6 nm, spherical overall, and were able to remain stable in different media for 72 h with drug loading up to 15.2%. The NVs were be successfully internalized within 6 h with good biocompatibility. Neither BHP nor NV showed significant toxicity when administered alone, however, BHP-NV demonstrated significant side effects in vitro and in vivo. The apoptosis rate increased significantly from 14.13% to 66.34%. Experiments in vivo showed that BHP-NV exhibited significant apoptotic and tumor-suppressive effects.

Conclusion: A targeted fluorescent NV with high drug delivery efficiency and sustained release protected the active center of BHP, constituting BHP-NV for targeted delivery. RPPMMRA demonstrated excellent biocompatibility, stability, and drug loading ability, whereas and BHP-NV demonstrated potent antitumor effects in vivo and in vitro.

Keywords: HPMA copolymers, BH3 domain, pro-apoptotic, polypeptide drugs, RGDfK

Introduction

Cancer is one of the leading causes of death worldwide, with no effective treatments available.[1] Antitumor polypeptides, including both small-molecule (molecular weight <1000) and protein drugs, are a powerful substitute for conventional small-molecule anticancer drugs.[2–4] Since the beginning of the century, peptides have been ideal candidates for alternative therapeutic options due to the urgent demand and their inherently high activity, small dosage, good solubility, excellent safety, uncomplicated synthesis, and modification.[5–11] However, almost all antitumor peptides exhibit low metabolic stability, poor specificity of tumor cells, and poor permeability of tumor tissues and cell membranes. This hinders the application of antitumor peptides in clinical treatment. As the theory of apoptosis becomes clear, the induction of tumor cell apoptosis specifically targeting the apoptotic pathway, can be an effective therapeutic

Received: 18 July 2023
Accepted: 13 September 2023
Published: 19 September 2023

Graphical Abstract

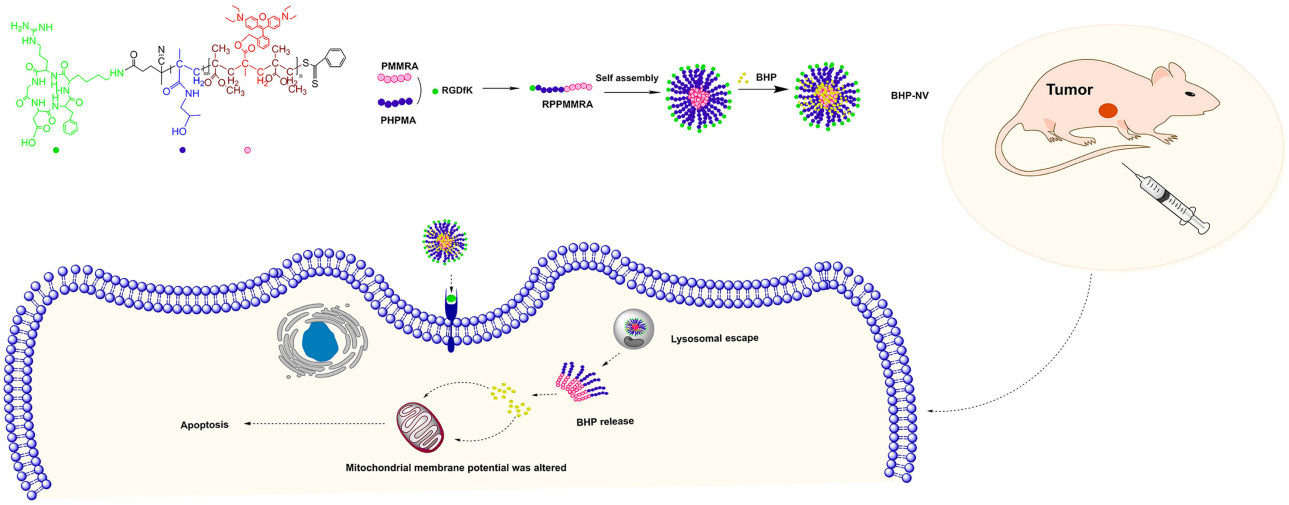

approach.[12] Peptides and their derivatives with apoptosis-inducing functions have gradually become important in the research and development of antitumor agents. BH3 peptides are derived from the Bcl-2 family and their analogs have demonstrated unique apoptotic activation functions.[13–17] In our previous study, we synthesized and evaluated a peptide containing 20 amino acid sequences depending on the Bax-BH3 domain, namely BHP, which could be considered a novel small-molecule anticancer peptide drug.[18] However, BHP is hindered by inefficacious cellular internalization and proteolytic resistance. The design of an appropriate drug carrier to deliver BHP and ensure its uptake by cells is a critical aspect of cancer treatment efficacy.[19–25]

Currently, polymeric nanovectors (NVs) are used to reduce the overall toxicity of drugs, enhance their solubility and biocompatibility, and are conducive to the treatment of various diseases, primarily focusing on anti-inflammatory, antineoplastic, arthritis, and other treatments.[19,26–28] Various polymeric vectors have been applied for the delivery of anti-arthritic treatments, among which PLGA and PEGylated vectors are more frequently used.[29] Hu et al utilized a grafted polymeric vector to deliver pMyD88, which has a certain anti-inflammatory ability, and effectively prolonged the survival time and reduced rejection in mice after liver transplantation.[30] Cui et al utilized RGD-PEG-PLys (CAA) carrier to deliver drugs for anti-glioma studies.[31] The hydrophilic end was exposed in the outermost layer of the system and the stability of the vector was determined. Hence, the skeletal structure of the hydrophilic end of the NV is essential. N-(2-hydroxypropyl) methacrylamide (HPMA) copolymers (PHPMA) have been studied for their biocompatibility, non-toxicity, non-immunogenicity, and long cycle times that allow drug delivery to target regions.[32–37] Simultaneously, PHPMA enhances the energy barrier for the adsorption of proteins or other biomacromolecules in blood circulation owing to the hydrophilic and tightly bound water layer of their polymer skeleton.[34,38,39] Therefore, PHPMA was selected for constructing the hydrophilic ends of the NV polymer.

Early solid tumors tend to have a higher blood vessel density than healthy tissues. This also offers favorable conditions for applying the enhanced permeability and retention (EPR) effect, facilitating the enrichment of the drug delivery system within the tumor area.[31] However, later solid tumors are mostly avascular and have certain coagulation properties, limiting the EPR effect.[40,41] The polymeric NV design should stably reach the target site irrespective of the targeting.[42] Cyclic RGD pentapeptide (Arg-Gly-Asp-Phe-Lys) (RGDfK) has high metabolic stability and selectively binds with $\alpha v\beta 3$ integrin that is overexpressed in angiogenic vessels and certain cancer cells with high affinity.[43–48] Liu et al successfully induced the conventional surface modification of liposomes using RGDfK cyclic peptide for the targeted delivery.[21,39] Therefore, RGDfK was selected as the targeting group of NV, depicting active targeting

characteristics. The stability of HPMA and the targeting ability of RGDfk were combined to ensure that NV could deliver BHP more efficiently.

Over the last 5 years, visualization therapy has received immense attention in the international field of nanobiomedicine, as it allows for real-time, accurate treatment, monitoring of efficacy, and adjustment of the drug regimen at any time during the treatment process, optimizing treatment effects while reducing toxicity and side effects.[49–56] Modified Rhodamine B (Rhob-MA) has been covalently polymerized as a fluorophore on NV; covalently, Rhodamine B may exhibit a high fluorescence signal.[23,57] Polymethylmethacrylate (PMMA) is the skeleton of the hydrophobic end and is often used for osteomyelitis, bone cement, antibiotic delivery, and other associated orthopedic diseases, leading to low toxicity.[58–61] RGDfK-PHPMA-b-Poly (MMA-*alt*-(Rhob-MA)) (RPPMMRA) is hydrophilic at one end and hydrophobic at the other and can self-assemble into spherical vesicles encapsulating BHP in water. This vector has potential for use in cancer visualization therapy because of the presence of covalently linked Rhob-MA and RGDfK.

Thus, we hypothesized that RPPMMRA, incorporating the tumor cell-targeted and active apoptotic protein BHP, namely BHP-NV, along with our experience in polymer biomaterial research and targeted drugs, would yield promising results.[62–64] BHP-NV compensates for the limitations of BHP, such as its inefficient cellular internalization and proteolysis resistance. BHP-NV offers a higher loading capacity and improved stability, along with protection against unwanted interactions and recognition events with vectors and proteins in the blood. Simultaneously, RGDfK targets tumor cells. Using a reverse docking simulation, BHP was found to have diverse therapeutic effects on tumors. This study demonstrated that BHP-NV was effectively internalized by A549 cells and induced apoptosis in vitro. It also demonstrated good biocompatibility and antitumor effects in vivo, indicating its potential as NV for therapeutic applications (Figure 1).

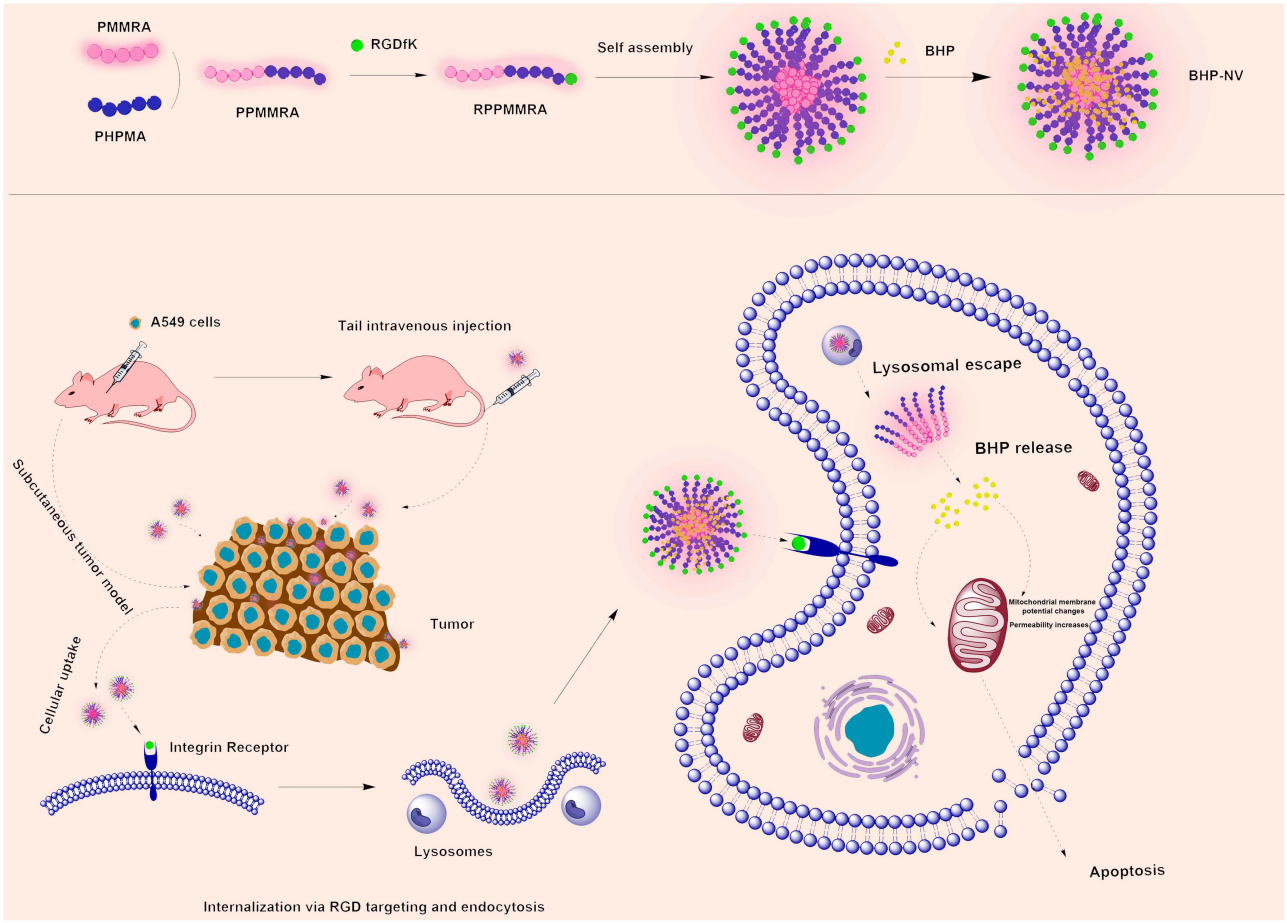

Figure 1 Schematic diagram for the preparation of the BHP-loaded polymeric nanovector BHP-NV and its application.

Materials and Methods

Materials

Methanol, ethanol, tetrahydrofuran (THF), anhydrous diethyl ether, dichloromethane (CH_2Cl_2), acetonitrile, triethylamine, concentrated hydrochloric acid (HCl), glacial acetic acid, petroleum ether, isopropyl alcohol, ethyl acetate, n-hexane, and methyl methacrylate (MMA) were obtained from Beijing Chemical Plant (Beijing, China). Rhodamine B (Rhob), sodium chloride (NaCl), elemental sulfur (S), anhydrous sodium sulfate (Na_2SO_4), sodium hydroxide (NaOH), disodium hydrogen phosphate (Na_2HPO_4), potassium dihydrogen phosphate (KH_2PO_4), 2-(N-morpholine) ethanesulfonic acid (MES), and azobisisobutyronitrile (AIBN) were purchased from Sinopharm Chemical Reagent (Beijing, China). Sodium methoxide, methylacryloyl chloride, and potassium ferricyanide were purchased from Shanghai Aladdin Bio-Chem Technology (Shanghai, China). Benzyl chloride, tetrahydroaluminum lithium ($LiAlH_4$), and 4,4′-Azobis (4-cyanovaleric acid) were purchased from Sigma-Aldrich (St. Louis, MO, USA). The RGDfK peptide and BHP with the DASTKKLSECLRRIGDELDS sequence were obtained from Gill Biochemical (Shanghai, China). Normal primary human umbilical vein endothelial cell line HUVEC and the human lung cancer cell line A549 were procured from the American Type Culture Collection (ATCC). Dulbecco's Modified Eagle's Medium (DMEM) was purchased from Gibco (Life Technologies). Fetal bovine serum (FBS) was purchased from KangYuan Biology (Tianjin, China) and MTT was obtained from Beyotime (Shanghai, China). The following detection kits were used: Annexin V-FITC/propidium iodide (PI) apoptosis detection kit and PI-based cell cycle detection kit from Bestbio (Shanghai, China); mitochondrial membrane potential assay kit with JC-1 probe from Beyotime (Shanghai, China); Lyso-Tracker Green from Beyotime (Shanghai, China); Hoechst 33342 from Beyotime (Shanghai, China); and crystal violet from Meilunbio (Dalian, China). All chemicals were used without further purification.

Rhob is Modified to Rhob-MA

Rhodamine B (1 g) was dissolved in THF (37.5 mL), and $LiAlH_4$ (0.2 g) was added. The mixture was stirred overnight at room temperature for 12 h under N_2 atmosphere. Water was added dropwise to quench the reaction. After filtration, the filtrate was extracted with dichloromethane, washed with a saturated NaCl solution, and dried over Na_2SO_4. Then, 60 mg of elemental sulfur (S) and reactant in the last step (100 mg) were mixed in a round-bottom flask and reacted at 160°C for 30 mins under N_2 protection and finally cooled to room temperature. Anhydrous ethanol (3 mL), concentrated hydrochloric acid (0.25 mL), and ultrapure water (6 mL) were added to the reactants. It was then extracted with dichloromethane, washed with a saturated NaCl solution, and dehydrated by adding Na_2SO_4. The crude product was obtained by vacuum drying. Rhob-OH was purified by column chromatography at a methylene chloride/methanol ratio of 9:1. Methylacryloyl chloride (25 mg), triethylamine (50 mg), and Rhob-OH (75 mg) were dissolved in dichloromethane. The reaction was performed overnight at room temperature, and the mixture was washed with distilled water and dried over Na_2SO_4. Vacuum drying and purification by column chromatography were performed to obtain methyl-propenyl-functionalized Rhodamine B (Rhob-MA). The ratio of the developing agents was methylene chloride: methanol=9:1.

Synthesis of RGDfK-PHPMA-b-Poly (MMA-Alt-(Rhob-MA)

Synthesis of 4-Cyanopentanoic Acid Dithiobenzoate (CPADB)

The synthesis of CPADB in this study was based on a previous work by Yoshiro et al[65] Typically, sodium methoxide (4.5 g), S (0.8 g), anhydrous methanol (6.25 g), and benzyl chloride (1.575 g), were used in the reaction, which was performed at 67 °C for 10 h. After the reaction, the mixture was cooled to 4°C in the ice bath and filtered before vacuum drying to remove the residual solvent. The reactants were dissolved in ultrapure water (12.5 mL), acidified using 1.0 mol/L HCl (12.5 mL), extracted thrice with ether (5 mL), and mixed with ultrapure water (7.5 mL). Then, a 1.0 mol/L NaOH solution (15 mL) was added to transfer the sodium dithiobenzoate to the aqueous phase. The resulting solution (8.75 mL) was mixed with aqueous solution (15 mL) of aqueous potassium ferricyanide (0.823 g, 2.5 mmol). The resulting red precipitate was filtered and cleaned with ultrapure water until the solution became colorless. The solids were dried overnight under a vacuum to obtain the crude products, which were then recrystallized and purified using ethanol.

Finally, CPADB was obtained by dissolving 4,4′-Azobis (4-cyanovaleric acid) (219 mg), and the product obtained in the previous step (160 mg) was dissolved in ethyl acetate (3 mL). The reaction solution was heated at reflux condensation for 18 h. The crude products were separated via column chromatography with ethyl acetate: n-hexane (2:3) as the eluent and vacuum-dried overnight. The product was purified by column chromatography at an ethyl acetate: n-hexane ratio of 2:3.

Synthesis of PMMRA

MMA (5 mL), CPADB (25 mg), AIBN (3 mg), and Rhob-MA (12 mg) were dissolved in 1,4 dioxane. Nitrogen protection was performed after three rounds of freeze-thaw degassing, and the reaction was carried out at 70°C for 6 h. Based on the study by Barsbay M and Anžlovar et al, CPADB was chosen as the chain transfer reagent for this reaction.[66,67] After completion of the reaction, the product was precipitated with petroleum ether. Purified PMMRA was obtained by vacuum drying overnight. In some experiments, red fluorescence interfered with the experimental results. Thus, a batch of non-fluorescent vectors was prepared using a similar method but without the addition of Rhob-MA.

Synthesis of PHPMA-b-Poly (MMA-*Alt*-(Rhob-MA)) (PPMMRA)

HPMA (50 mg), AIBN (3 mg), and PMMRA (36 mg) were obtained in the previous step. Nitrogen protection was completed after freeze-thaw degassing three times, and the reaction stayed overnight at 70°C in 1,4 dioxane. After completion of the reaction, the product was precipitated with diethyl ether. The purified product PPMMRA was obtained by vacuum drying. Based on Utama et al, it is feasible to use HPMA as the hydrophilic end and CPADB for the RAFT polymerization reaction.[68]

Synthesis of RPPMMRA

NHS (0.5 mg), EDC (0.8 mg), and PPMMRA (26 mg) were dissolved in the MES buffer for 24 h at room temperature. NHS-PHPMA-b-Poly (MMA-*alt*-(Rhob-MA)) (N-PPMMRA) was synthesized. RGDfK (8 mg) was allowed to react in MES buffer at room temperature for 24 h. Purified RPPMMRA was obtained by freeze-drying the product solution for 48 h after purification via dialysis.

The Self-Assembled BHP-NV

The preparation of BHP-NV can be explained using the self-assembly of RPPMMRA@BHP as an example. The dried RPPMMRA block copolymer (4 mg) was dissolved in THF (1 mL). In addition, BHP (5 mg) was dissolved in pure water (10 mg). The polymer solution was then added dropwise onto the BHP solution and ultrasonicated for 15 min. The drug loaded vector RPPMMRA@BHP was obtained via vacuum rotary evaporation at 50°C until the solvent was free.

BHP-NV Morphological Observation and Stability Test

The prepared BHP-NVs and the NVs were then tested. First, the hydration particle size and dispersion of the product were measured using a Malvern particle size analyzer. Moreover, the morphology of the BHP-NVs was observed using transmission electron microscopy. The aqueous solution was freeze-dried to obtain a powdered product, which was then weighed and dissolved under different conditions for stability testing. The stability in different solution states was tested for 72 h at 25°C. Samples were analyzed at specific time points using a Malvern particle size analyzer.

Determination of Drug Loading, Encapsulation Rate, and Drug Release Curve of Polymeric Nanovector

Drug release assays were performed by placing 10 mg/mL BHP-NV into a dialysis bag with a molecular weight cut of (MWCO) = 2000 Da at 37°C. PBS (pH 7.4, 2000 mL) was used as the release medium. Samples of 20 mL were collected at 0, 6, 12, 24, 48, and 72 h and replenished with the same volume of PBS. The drug loading and encapsulation efficiency of the BHP-NV was determined using high performance liquid chromatography (HPLC) on the C18 column (5 μ 250×4.6 mm) at 35°C. The mobile phase was A: 0.1% trifluoroacetic in 100% water, B: 0.1% trifluoroacetic in 100% acetonitrile, the flow rate was 1.0 mL/min, the detection wavelength was 220 nm, and the sample volume was 10 μL. BHP solutions was prepared at concentrations of 1175, 1000, 500, 250, and 100 μg/mL. The HPLC experiments were performed using the chromatographic column conditions described above.

Determination of Hemolytic Activity of Nanovectors and Peptides

Fresh blood samples (1–2 mL) from healthy participants were collected in EDTA anticoagulant tubes, rinsed with an equal volume of PBS, centrifuged at 1000 rpm for 5 min, and the supernatant was discarded. This procedure was repeated four times to obtain colorless supernatants. Next, 1 mL of centrifuged human red blood cells (RBCs) was collected and 20 times the volume of PBS was added for resuspension, counting, and adjusting the suspension concentration to 2×10^8/mL RBCs. The samples were dissolved with PBS prepared using different concentration gradients, and then successfully added to the 96-well U-shaped plate using 70 μL per well with three parallel settings for each concentration. Approximately 70 μL red blood cell suspension was added to each well of a 96-well U-shaped plate with a round bottom. The negative and positive control groups were set and incubated at 37°C for 2 h with 90 rpm shock. The 96-well plates were centrifuged at 3000 rpm at 4°C for 5 min, 90 μL supernatant was removed from the 96-well plate into the flat bottom, and the absorbance was tested at 578 nm.

Drug hemolysis and hemolysis rates were determined. Hemolytic toxicity occurs when the hemolysis rate exceeds 10%. The minimum drug concentration that leads to RBC hemolysis is known as the minimum hemolysis concentration.

$$Hemolysis\ ratio\ (\%)=\frac{A-A_{PBS}}{A_{water}-A_{PBS}}\times100\% \tag{1}$$

Carrier Cell Internalization Experiment

A549 cells were evenly spread onto six-well plates at a density of 2×10^5 cells per well. After 24 h culture in DMEM complete medium at 37°C with 5% CO_2, DMEM medium with 100 μg/mL PPMMRA was incubated at different times. Hoechst 33342 blue dye was used to stain the nuclei. Fluorescence microscopy was used to confirm these observations.

Drug Toxicity Test by 3-(4,5-Dimethylthiazol-2-Yl)-2,5-Diphenyltetrazolium Bromide (MTT) Method

After the digestion of A549 cells with 0.25% trypsin, complete DMEM was added to terminate the digestion. The cells were then resuspended in a single-cell suspension. The culture medium of 1×10^4 cells per well was inoculated in a 96-well plate at 37°C under 5% CO_2 for 24 h.

$$Cell\ viability=\frac{A_e-A_0}{A_c-A_0}\times100\% \tag{2}$$

BHP-NV Induced Apoptosis Experiment

A549 cells were re-inoculated into six-well plates at a density of 2×10^4 cells per well and incubated under different conditions. After 24 h, the cells were digested with 0.25% (w/v) trypsin and centrifuged. The Annexin V-FITC/PI kit dye was used for 30 mins at 4°C in the dark. The stained cells were collected by centrifugation, and the excess staining fluid was removed. The cells were suspended in PBS and the fluorescence of each cell was analyzed using flow cytometry. Finally, apoptosis of apoptotic cells was analyzed using BD CellQuest Pro software. The experiments were repeated thrice for each group.

Analysis and Detection of Apoptosis Morphology

A549 cells were re-inoculated into a laser confocal culture dish at a cell density of 1×10^5 cells and cultured in a CO_2 incubator at 37°C and relative humidity of 5%. Cells were treated with different drugs for 24 h at a density of 80%. Then, 5 μg/mL of Hoechst 33342 dye was added to each plate. The cells were incubated at 37°C for 20 min without light and washed thrice using PBS.

Detection of Intracellular Mitochondrial Transmembrane Potential (MMP)

A549 cells were inoculated in six-well plates at a density of 2×10^5 cells per well. When the cell density reached 80%–90%, BHP, NV, and BHP-NV were administered for 24 h. JC-1 staining solution of 10 μM was added to each well and

treated for 20 min at 37°C under dark conditions. The PBS solution was washed thrice to remove the remaining dyes. A fluorescence microscope was used to observe the changes in the fluorescence intensity of each group of cells. ImageJ software was used to quantitatively analyze changes in the red and green fluorescence intensities of the cells. This experiment was repeated thrice.

Cell Colony Formation Experiment

After the A549 cells were digested using 0.25% trypsin, they were re-inoculated into each well of a six-well plate at 2×10^5 cells per well and treated with different drugs for 24 h for 7-d culture. Then, the waste medium was abandoned, and 1 mL of precooled 70% (v/v) ethanol was added to each well and fixed at 4°C for 20 min. Ethanol was absorbed and stained with a 0.2% crystal violet solution at room temperature for 15 min. The cells were then flushed with crystal violet and washed three times with PBS. Finally, the colony formation was observed and photographed under a fluorescence microscope. The ImageJ software was used to quantify the experimental results.

Lysosomal Escape Assay

A549 cells were re-inoculated into a laser confocal petri dish at 1×10^5 cells density and cultured at 37°C, inside a 5% CO_2 incubator. The culture medium was removed when the cells reached 80% confluence. The cell culture medium containing the fluorescent carriers was removed after the addition of PPMMRA, and the cells were incubated for different periods. The cells were washed thrice using PBS and replaced with 100 μm Lyso-Tracker Green staining solution. It was preincubated at 37°C, and the cells were co-incubated at 37°C for 30 min under dark conditions. Lyso-Tracker Green staining solution was removed, cleansed using PBS thrice, incubated with Hoechst 33342 dye at 37°C for 20 min without light, washed using PBS thrice, and observed under a confocal laser microscope.

Reverse Molecular Docking

The potential target proteins of BHP were predicted by reverse docking with PharmMapper (http://www.lilab-ecust.cn/pharmmapper/index.html) server, Version 2017. Cancer-related genes were identified and screened using the OMIM (https://omim.org), DRUGBANK (https://www.drugbank.com) and GeneCards (https://www.genecards.org) databases. Duplicate genes were removed by integrating the data from both databases to create a dataset containing diseases target information. Furthermore, relevant target genes were processed using the Uniprot database (https://legacy.uniprot.org/).[69–71] The PPI network was constructed using Cytoscape 3.9.1 software to visualize the targets obtained from the above steps. GO biological functions and KEGG pathway enrichment analysis of core targets were performed using the Metascape database (https://metascape.org/) and subsequently mapped using bioinformatics (http://www.bioinformatics.com.cn/).[72] All data were accessed on website in March-April 2023.

Antitumor Effect in A549-Bearing Nude Mice

All animal experimental protocols were performed in accordance with Guidelines for ethical review of animal welfare. This study was approved by the Institutional Animal Ethics Committee of Jilin University, Jilin, China (Approval No. 20220802). Rodents were free to eat sterilized food and drink distilled water and were housed in stainless steel cages containing hardwood chips, with all of the above in a barrier environment. For the mouse subcutaneous tumor model, 5–6 weeks old BALB/c female nude mice (both from Charles River, Beijing, China) were injected with 1×10^6 A549 cells per mouse within the right axilla (suspended in 100 μL sterile normal saline). The sizes of the subcutaneous tumors were determined using calipers. Twenty-five mice (18 ± 1 g) were randomly assigned into five groups (n = 5) and intravenously treated with: normal saline (100 μL), BHP (100 μL, 1 mg/mL in saline), RPPMMRA (100 μL, 1 mg/mL in saline), BHP-NV L (100 μL, 10 mg/mL BHP-NV in saline), BHP-NV H (100 μL, 20 mg/mL BHP-NV in saline) per mouse when the average tumor volume reached 50–100 mm^3. Saline-treated mice were used as the controls. When saline and samples were injected, the tumor sizes and mouse weights were periodically monitored. The tumors, hearts, livers, spleens, lungs, and kidneys of mice in all groups were harvested after 21 days of treatment, fixed in 4% paraformaldehyde solution, embedded in paraffin, and dissected into slices. Apoptosis in the tumor areas was estimated

using a TUNEL assay. Histological slices were stained with hematoxylin and eosin (H&E) and observed under a light microscope.

Results and Discussion

Synthesis and Characterization of Polymeric Nanovector RPPMMRA

NVs were prepared via Reversible Addition-Fragmentation Chain Transfer Polymerization (RAFT). The preparation process is described in the Materials and Methods. A general structural equation is shown in Figure 2. Amphiphilic NVs with one fluorescent hydrophobic end and another RGD-targeted hydrophilic end were prepared, as shown in Figure 2.

In this study, Rhodamine B modified with a methyl acryloyl group, Rhob-MA, was used to synthesize Rhodamine B polymerized onto nanoparticles in a controlled manner (Figures S1 and S2), and the content of Rhodamine B in PPMMRA vector was shown in Table S1. Modification of the carboxyl group in the structure of rhodamine B may influence the properties of the dye. The influence of the fluorescence intensity of the dyes at different pH values was analyzed, and the results are shown in Figure 3A (Rhodamine B) and Figure 3B (Rhob-MA); a standard curve of Rhodamine B fluorescence intensity and fluorescence emission spectrum of RPPMMRA are shown in Figure S3. As shown in Figure 3A, the fluorescence intensity in the emission spectrum of Rhodamine B increased as the pH increased from 5 to 8. However, the fluorescence intensity of Rhob-MA remained unaffected by pH because the replacement of

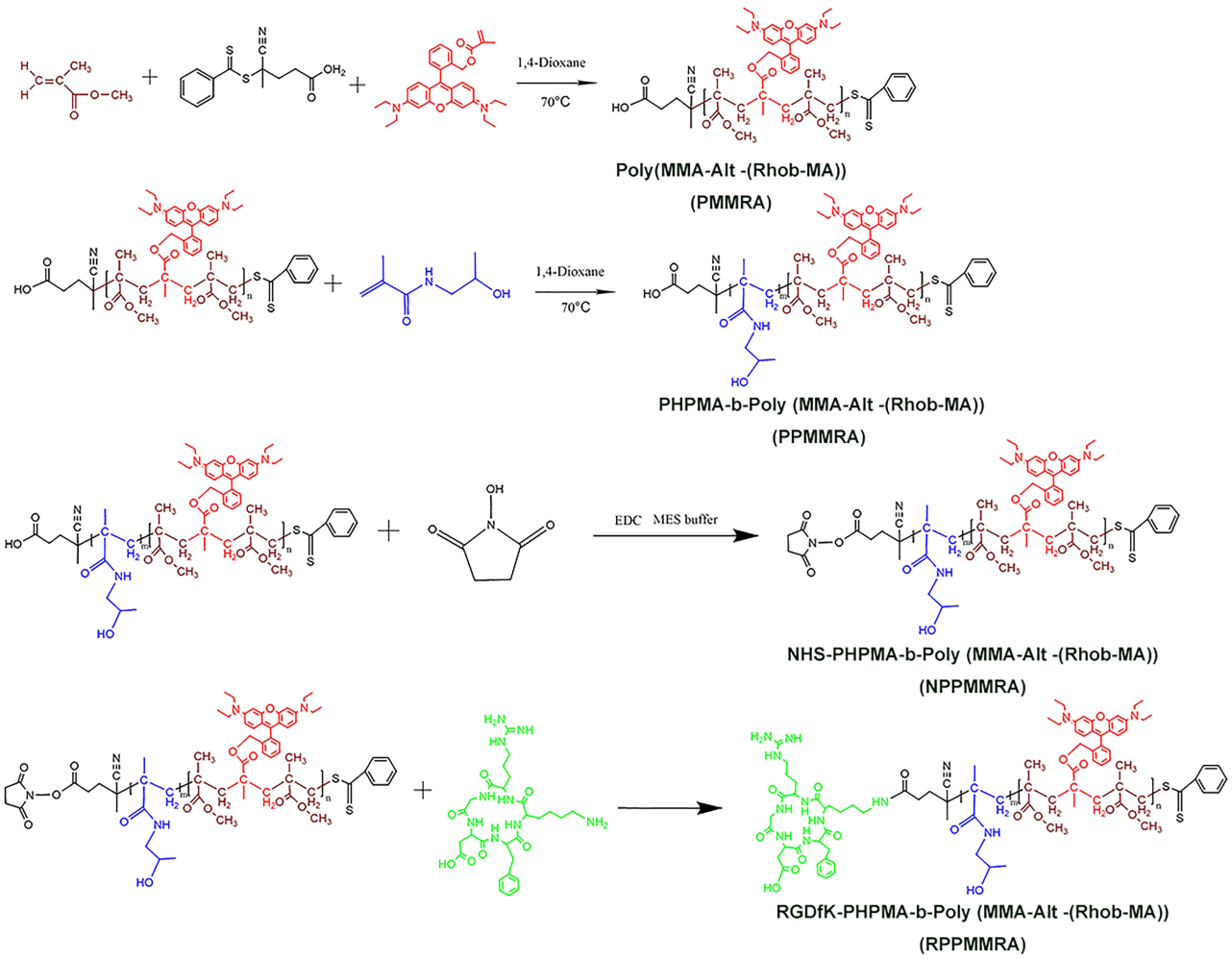

Figure 2 Synthesis strategy of polymeric nanovector RPPMMRA. The hydrophobic fluorescent PMMRA was prepared first, and the amphiphilic PPMMRA was obtained by polymerizing the HPMA monomer to the product. By linking RGDfK to the product PPMMRA with NHS, the targeting RPPMMRA was obtained. Methods described the specific synthesis strategy.

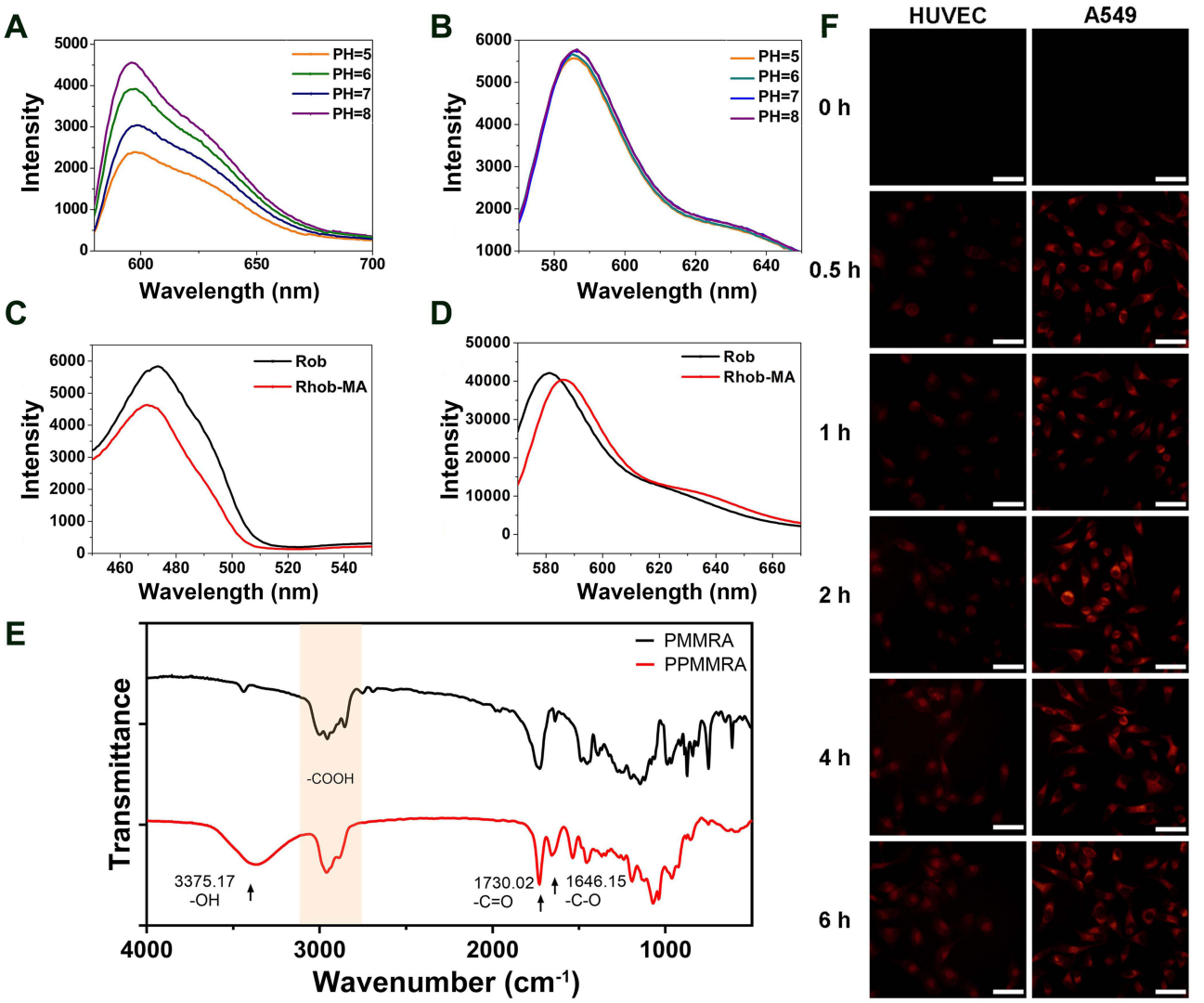

Figure 3 Analysis of fluorescence properties of modified Rhodamine B and polymeric nanovector characterization spectrum. (**A**) Emission spectra of Rhob at different pH. (**B**) Emission spectra of Rhob-MA at different pH. (**C**) Excitation spectra of Rhob and Rhob-MA at pH 7.4. (**D**) Emission spectra of Rhob and Rhob-MA at pH 7.4. (**E**) FTIR spectrum of PMMRA and PPMMRA. (**F**) Fluorescence microscopy images of HUVECs and A549 cells exposed to polymeric nanovector with RGDfK. Scale bars: 50 μm.

Rhodamine B with carboxyl methyl allyl weakened the influence of pH on the fluorescence intensity of Rhodamine B. This indicated that the polymeric fluorescence intensity of the drug-loaded nanoparticles could be stabilized in a variable pH environment, facilitating further observed intake (Figure 3B). The excitation and emission wavelengths of the dyes were measured at pH 7.4, and the results are shown in Figure 3C and D. The excitation and emission wavelengths of the two dyes were similar, and functionalization of the methyl acrylate group had no significant effect on the wavelength of the dye. The results indicated that the replacement of the hydroxyl group had no noticeable effect on its optical properties but decreased its sensitivity to the pH value. The fluorescence emission spectra of RPPMMRA and Rhob-MA mass spectral are shown in the Supporting Information.

Hydrophilic HPMA was polymerized into the product of the previous step to obtain the amphiphilic chain polymer PPMMRA after successful preparation of the hydrophobic end. The hydroxyl groups on the HPMA monomer product were characterized using infrared spectroscopy (Figure 3E).

The polymer contains carboxyl groups at its hydrophobic ends (Figure 3E). Thus, the FTIR spectrum of PMMRA has a peak at 3375.17 cm^{-1} with a wide and scattered characteristic peak at 2700–3000 cm^{-1}. This can also be referred to as the O-H in the carboxyl group of the polymer. After the polymerization of HPMA, the characteristic peak at

3375.17 cm^{-1} revealed a wide peak owing to the coexistence of the hydroxyl group on the HPMA monomer and the carboxyl group inside the polymer. This confirmed the successful preparation of PPMMRA. We characterized the prepared NVs using ^{1}HNMR. The experimental results are shown in Figures S4–S6.

The balance between the use of a chemical substance for medical purposes is so fragile that it can shift unpredictably between therapeutic efficacy and a range of toxicity.[73] Subsequently, two types of cells were selected to verify the targeting of RGDfK, cancer cell A549 (αvβ3-high expression) with high expression of αvβ3 integrin and normal HUVEC (αvβ3-low expression) with low expression of αvβ3 integrin. As demonstrated in Figure 3F, the fluorescence intensity and speed of NV were stronger in A549 cells than those in HUVECs. Moreover, the uptake of A549 cells was fast, with evident fluorescence within 0.5 h and stable fluorescence intensity. Thus, RPPMMRA containing RGDfK was successfully prepared with a selectivity of RGDfK against cancer cells.

Therefore, we have successfully prepared the NVs with stable fluorescence and high affinity for αvβ3 highly expressed in various tumor cells. Additionally, it can be widely used in the treatment of various cancers. These properties make the prospect of NVs application worthwhile.

Characteristics of Different Polymeric Nanovectors and BHP-NV

RGDfK may have a specific influence on the self-assembly of NVs. Two NVs, PPMMRA (without RGDfK) and RPPMMRA (with RGDfK), were selected for property evaluation. Two types of BHP-NVs were prepared: PPMMRA@BHP and RPPMMRA@BHP. The morphological characterization of the NVs is shown in Figures 4A–D. The TEM results are shown in Figures 4A (PPMMRA) and Figure 4C (RPPMMRA), illustrating that the NVs exhibited a spherical shape with a rough surface and had a particle size of approximately 100–150 nm. BHP can be loaded in large quantities at the interstices of NVs to effectively control drug release. We also analyzed the hydration particle size distributions of the two types of NVs and BHP-NVs (Figures 4B and D). The Z-average particle sizes of PPMMRA (Figure 4B) and RPPMMRA (Figure 4D) were 224.8 nm and 189.6 nm, respectively. The polydispersity index of the NVs was <0.24, indicating good dispersion. The particle size of the NVs increased after BHP loading owing to their presence in the NV interstices, thereby increasing the final particle size of BHP-NV. After linking with RGDfK, the NV particle size decreased because of increased hydrophilicity at the hydrophilic end of the molecule.

Nonspecific interactions with proteins and other molecules in the blood can affect the circulation time of BHP-NV owing to its practical application. Thus, it is also one of the factors that determines whether BHP can be effectively released in targeted cells and even in vivo. Therefore, it is important to investigate the stability of BHP-NV by simulating proteins in plasma and serum. We designed and synthesized another NV using hydrophilic PEG (PEGMMRA) as the shell instead of PHPMA to evaluate the stability of PHPMA in the outer part of the NV (Figure S7). After 72 h of incubation under different conditions, the PEGMMRA particle size was approximately 300% of the initial size. In contrast, the particle size of PPMMRA did not change significantly (Figure 4E and F). These results demonstrate that PPMMRA does not easily bind to serum and avoids increasing the particle size. Therefore, it can stably and effectively transport drugs, making it an ideal nanodrug vector.

Drug Delivery and Release Capacity

Mass spectrometry of BHP revealed a molecular weight of 2331 Da, which was consistent with theoretical calculations (Figure 5A). The sequence of BHP was DASTKKLSECLRRIGDELDS. The HPLC results for BHP at different concentrations are shown in Figure 5B. The peak time (19.6 minutes) and peak area were positively associated with concentration. Figure 5C shows a standard curve to determine the encapsulation rate and drug loading capacity of the two BHP-NV samples.

As shown in Figures 4B and D, the particle size of the BHP-NVs increased after BHP loading. The particle sizes of the NVs increased to 114.1% (PPMMRA) and 129.3% (RPPMMRA). Two BHP-NV samples were used to measure drug loading and explore whether particle size enlargement was related to drug loading. The BHP release curves and loads are shown in Figure 5D. The encapsulation rates of RPPMMRA@BHP and PPMMRA@BHP were 14.0% and 11.0%, respectively. Moreover, the drug-loading amounts were 15.2% and 9.1%, respectively. RPPMMRA@BHP showed better drug loading, and the increase in size after BHP loading was prominent. This indicates that there may be a specific

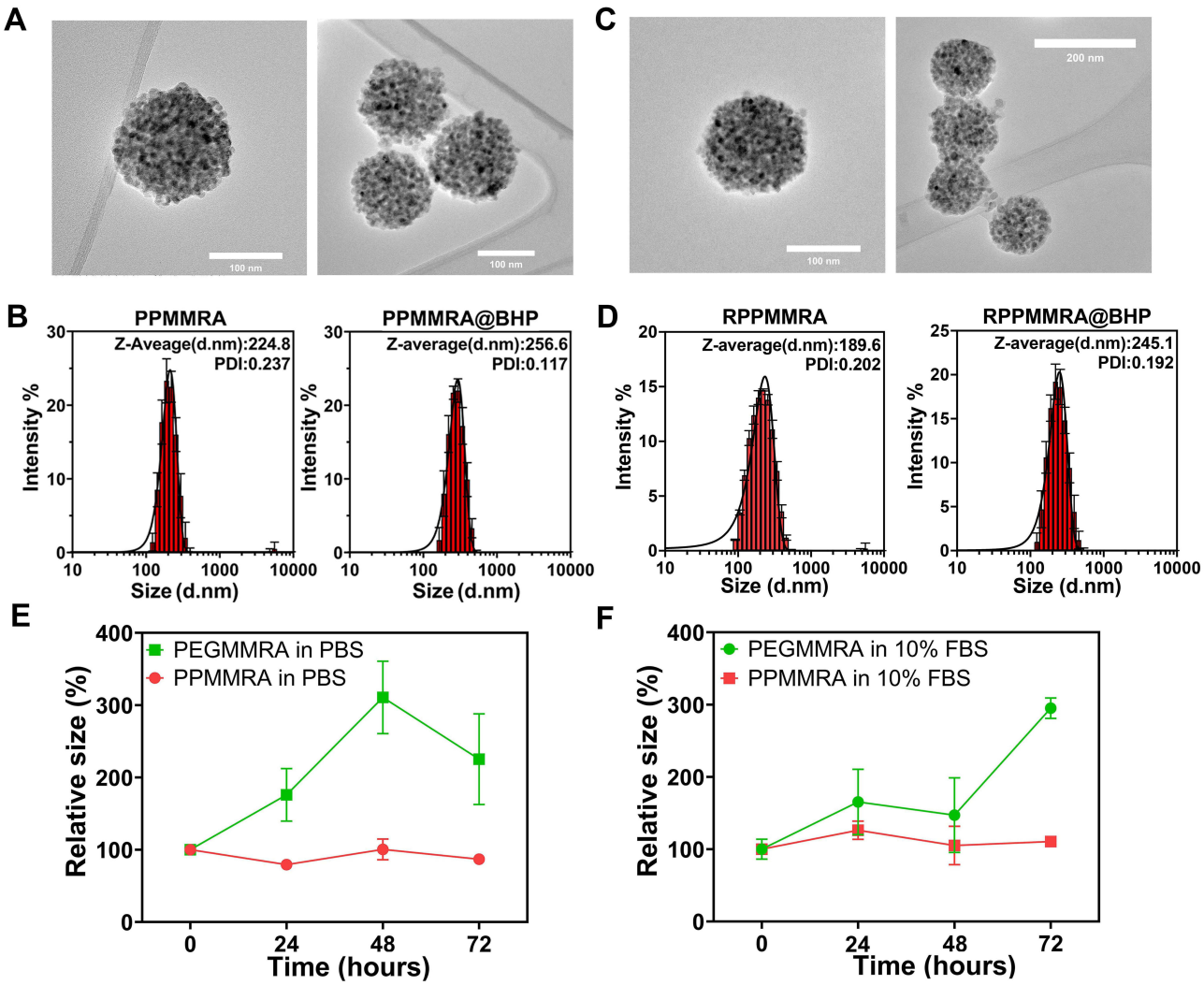

Figure 4 Characteristics of different polymeric nanovectors and BHP-NV. (**A**) TEM image of PPMMRA (without RGD). (**B**) Size distribution of PPMMRA after BHP loading. (**C**) TEM image of RPPMMRA (with RGD). (**D**) Size distribution of RPPMMRA after BHP loading. (**E**) Stability of different NVs in PBS. (**F**) Stability of different NVs in medium containing 10% serum.

correlation between the drug loading amount and the size increase. The release rate of BHP-NV was approximately 80.0% at 48 h and was almost completely released at 72 h, as observed in the drug release curve. This release property protects BHP from premature release into the circulation during vector delivery. Premature drug release often leads to off-target toxicity in the delivery system, which has always been avoided. Owing to the properties of the vector, the release effect lasts longer and has specific application potential. RPPMMRA has better drug delivery capacity and active targeting of RGD than PPMMRA, which can load and release BHP in cells more effectively. Therefore, RPPMMMRA is referred to as NV. NVs are powerful alternatives for future clinical therapies owing to their ability to prevent drug degradation, better guide to target locations, and diverse and flexible properties through different functional groups.[74]

Biocompatibility, Toxicity, and Cellular Uptake Experiments

Good biocompatibility is an essential factor in nanomaterial therapy, and hemolysis tests can establish the biological safety of a material. As described in Figures S8 and 6A, both PMMA and NVs had negligible destructiveness to RBCs. Our peptide drug, BHP, also caused insignificant RBC damage at concentrations up to 200 μg/mL (Figure 6B). This demonstrated the good biocompatibility of NVs and their promising applications in drug delivery and controlled release. In our previous study, Au-NPs were used for the delivery of anticancer drugs, and demonstrated good cellular non-

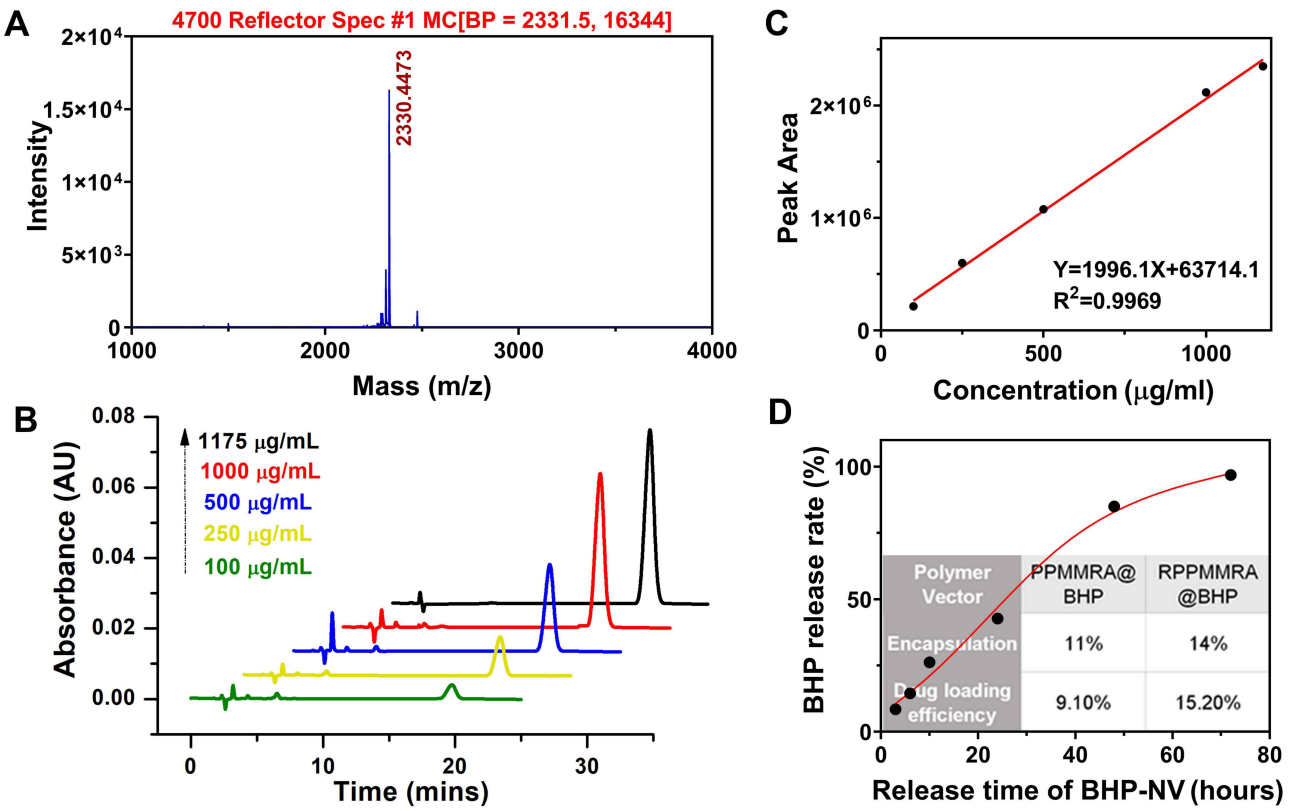

Figure 5 Drug delivery and release capacity of the BHP-NV complex. (**A**) Time of flight mass spectrometry of BHP. (**B**) HPLC of BHP with different concentrations. (**C**) The standard curve was drawn based on the peak area of HPLC and the concentration of BHP. (**D**) Drug release curve and encapsulation rate and drug loading of BHP-NV.

toxicity. Green nanotechnology, which can extract Au-NPs from onions, making their preparation much less expensive, is a promising alternative.[75]

Highly cytotoxic vectors can destroy healthy cells and cause severe toxic side effects during intracellular delivery. Therefore, low vector toxicity is crucial for safe and effective drug delivery. A MTT assay was used to detect the effects of BHP, NV, and BHP-NV on cell viability. As shown in Figure 6C, high cell viability was observed after incubation with BHP and NV up to 1000 μg/mL and 400 μg/mL, respectively, for 24 h. This indicates that the biocompatibility of NV is relatively safe, with little effect on the cells. Subsequently, cell viability significantly decreased in the BHP-NV treatment group compared to that in the NV treatment group (Figure 6D). Thus, with an increase in BHP-NV concentration, the cell apoptosis rate increased progressively, because of the sustained drug release effect of BHP-NV. Significantly, the BHP-NV treatment group had superior cell-killing ability, which was attributed to BHP with 20 amino acids that could inhibit the survival and growth of A549 cells with pro-apoptotic activity.

The fluorescence intensity of the NVs in A549 cells was recorded to visually observe the NVs of the multifunctional supramolecular nanomaterials. Red fluorescence of Rhodamine B was observed in A549 cells after incubation with NV for 0.5 h and increased with increasing incubation time (Figure 6E and S13), indicating that NV was internalized into the cells. Red fluorescence of the NV and blue fluorescence of the cell nuclei demonstrated that RPPMMRA entered the cells. No apparent damage was observed in the nuclei, after continuous incubation for 6 h, as indicated by blue fluorescence. This indicates that we successfully synthesized a new, nearly non-toxic nanodrug carrier. Simultaneously, NVs were successfully released from the lysosomes after entering the cell (Figure S10).

In vitro Antitumor Efficacy

Numerous studies have shown that mitochondria are closely associated with apoptosis, and a decrease in the MMP is an early event in the apoptosis cascade. This occurred before the appearance of nuclear apoptosis (chromatin concentration

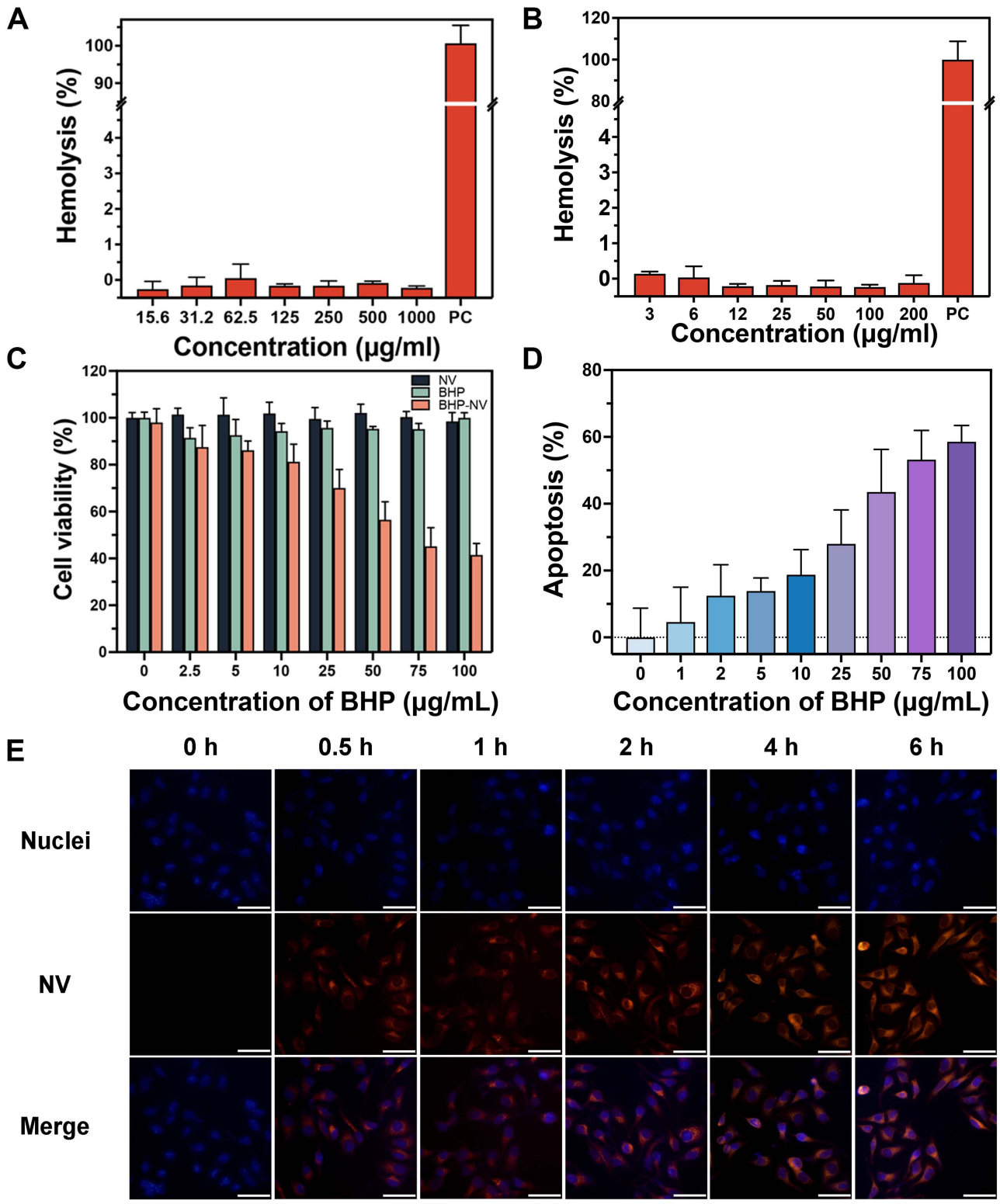

Figure 6 Hemolysis test of various materials: (**A**) NV and (**B**) BHP (PC: positive control group). In vitro cytotoxicity of (**C**) NVs, BHP and BHP-NV against A549 cells at different concentrations after 24 h. (**D**) The apoptosis of BHP-NV calculated from cell viability against A549 cells after 24 h. Data represent mean values ± standard deviation, n = 6. (**E**) Cellular internalization of 100 μg/mL NV by A549 cells at 37°C for 0, 0.5, 1, 2, 4, and 6 h. The cell nuclei were stained as blue by Hoechst 33342, red was the fluorescence of RPPMMRA. Scale bar: 50 μm.

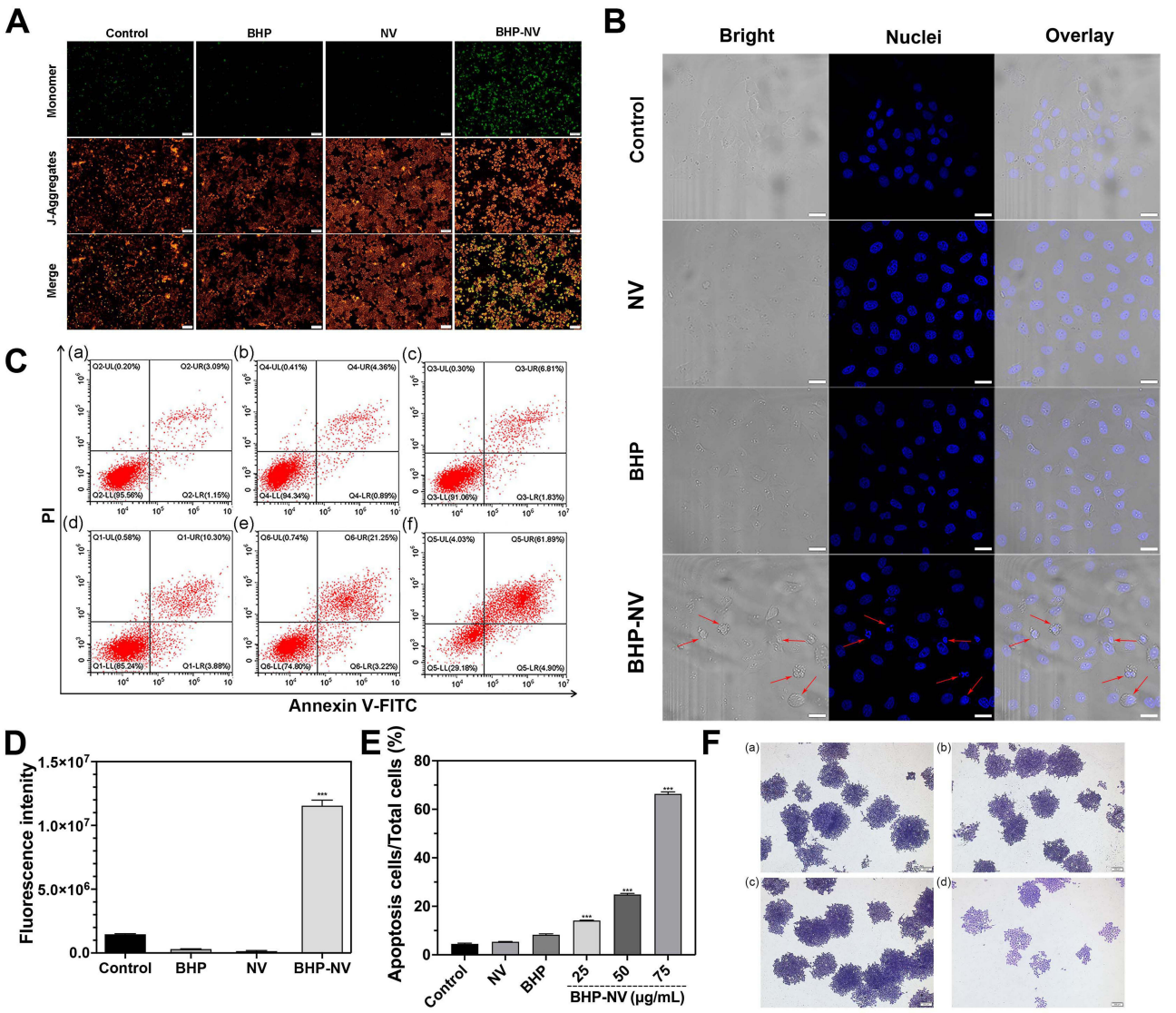

Figure 7 In vitro antitumor efficacy. (**A**) Detection of the mitochondrial membrane potential of A549 cells after treatment with BHP, NV, and BHP-NV; the concentration of proteins was 50 μg/mL. Scale bar: 100 μm. (**B**) Apoptosis visualization. CLSM images of A549 cells incubated with BHP-NV for 24 h, the cell nuclei were stained as blue by Hoechst 33342, and the concentration of proteins was 50 μg/mL. Scale bar: 20 μm. (**C**) Flow cytometry assay for apoptosis of A549 treated with (a) Control, (b) NVs (without Rhob-MA), (c) BHP, (d) 25 μg/mL BHP-NV, (e) 50 μg/mL BHP-NV and (f) 75 μg/mL BHP-NV, the concentrations were peptide content. (**D**) Numerical data present the ratio of monomer to J-aggregates fluorescence intensity from (**A**) and (**E**) the ratio of apoptosis cells to total cells from (**C**). (n = 3) (**F**) The effect of different treatments on cell colony formation. (a) Control, (b) BHP, (c) NVs, and (d) BHP-NV. Scale bar: 200 μm. Significant difference is presented as ***, indicating $p < 0.001$.

and DNA fragmentation). Once the MMP collapses, apoptosis becomes irreversible. Figures 7A and D show that the cells were in good condition, with weak cell membrane permeability in the Control, BHP, and NV groups (without Rhob-MA). The MMP was normal, and the fluorescent probe JC-1 entered the mitochondria via mitochondrial membrane polarity. In the BHP-NV group, pro-apoptotic BHP was loaded into the cells, resulting in cell damage, structural destruction, and apoptotic mitochondria.

Flow cytometry was used to detect cell apoptosis after administration to investigate the effect of the BHP-NV complex on cell apoptosis. The cell apoptosis experiments indicated that the BHP-loaded complex had a higher apoptosis-inducing ability than the empty NV and BHP groups (Figures 7C and E). Apoptosis could be significantly increased from 14.1% to 66.3% with the increase in drug concentration from 25 μg to 75 μg. This was similar to the results obtained from the MTT assay, indicating that the BHP-NV nanodrug could induce tumor cell apoptosis. NVs can successfully load BHP, which has a pro-apoptotic effect on cells, thereby inhibiting cell proliferation.

Similarly, the impact of BHP-NV on cancer cell apoptosis can be estimated by staining the nucleus and observing the cell morphology in a bright field. Morphological changes due to apoptosis were observed in each group using laser confocal microscopy. When apoptosis occurs, the cell morphology is anomalous. Apoptotic cells were round, the cell volume was decreased, the nucleus was deeply stained, the cytoplasm was concentrated, and cell surface buds appeared. The nucleus was cleaved into several fragments, and several apoptotic bodies with intact membrane structures were formed in the cytoplasm, as shown in Figures 7B and S9, which is consistent with previous data.

Colony formation is an effective procedure to detect the proliferative ability of cultured cells. As shown in Figures 7F and S11, BHP-NV significantly reduced the cell colony formation ability. In contrast, neither the NV nor BHP inhibited cell proliferation. The results indicated that our vector had no significant effect on the inhibition of cell proliferation compared with the other groups. The BHP-NV group inhibited the proliferation of A549 cells in the cell clone formation experiment, indicating that BHP loaded with NVs significantly reduced cell clone formation.

Reverse Molecular Docking to Explore the Potential Therapeutic Effect of BHP

Reverse molecular docking technology is a computer-aided drug design technology that supports reverse pharmacophore matching and is economical and convenient for locating new targets of medicine, explaining the molecular mechanism of medication and drug repositioning to seek out alternative indications of drugs, as well as detecting adverse drug reactions and drug toxicity. First, the BHP structure was imported into the Superpred and PharmMapper servers for reverse protein target prediction analysis, 450 targets with Norm Fit > 0.2348 and Superpred Probability > 50% were screened out, and then based on the DRUGBANK, OMIM, and GeneCards correlation scores of > 20%, a total of 915 disease targets were screened out. Finally, 76 targets retained intact after duplicate targets were removed, as shown in Figure 8A and Table S2. Protein targets often function through protein-protein interactions; therefore, it is necessary to construct PPI networks. The obtained intersecting targets were used to build a PPI network for BHP anticancer activity using Cytoscape software (Figure S12). In this network, the size of the node and shade of color represent the magnitude of the degree value; a larger node and darker color indicating the higher node degree value. Epidermal growth factor receptor (EGFR), HRAS (GTPase HRas), and AKT1 (RAC-alpha serine/threonine-protein kinase) among others, occupied an important position in the network, indicating that these target proteins play important roles in the treatment of tumors by BHP.

Subsequently, GO and KEGG enrichment analyses were performed using the 76 anticancer targets of BHP (Figure 8B and C). According to GO classification, three domains were covered: cellular components (CC), biological processes (BP), and molecular functions (MF). In the BP domain, the enriched regions included the transmembrane receptor protein tyrosine kinase, cell population proliferation, programmed cell death, and regulation of apoptosis. Among the MF domains, protein kinase binding, protein tyrosine kinase, and protein homodimerization activities were affected. KEGG bubble plots showed only 20 enriched pathways based on core targets with p-value<0.01 and count>10, where the larger the enrichment factor, the greater the degree of enrichment. BHP treatment affects diverse pathways, primarily those related to cancer and immune-related signaling pathways, such as the p53 and IL-17 signaling pathways. It is speculated that BHP plays an important role in tumor therapy by regulating these pathways.

To visualize the relationship between the BHP peptide, targets, and diseases in a simple and direct manner, a peptide-target-disease network diagram (Figure 8D) was constructed using Cytoscape, where red represents the BHP peptide, green represents potential gene targets associated with BHP and diseases, and blue represents cancer-related diseases. This illustrates that BHP has potential therapeutic effects on a variety of cancers such as gastrointestinal neoplasms, adenocarcinoma, breast neoplasms, and prostatic neoplasms, furture demonstrating the feasibility of BHP nanodrug.

In vivo Tumor Inhibition Performance

We conducted in vivo inhibition of BHP-NV in mice bearing A549 tumors after stimulation with BHP-NV, owing to its excellent antitumor capacity in vitro. In this study, tail vein injection was used to evaluate tumor retention of the polyplex. Two doses of BHP-NV were used in this study: BHP-NV L and BHP-NV H. The specific concentrations are described in the Methods section. After the BHP-NV injection, we monitored the body weight and tumor volume of the mice. The tumor tissues separated from the different treatment groups after 20 days are shown in Figures 9A and S14. Figure 9B indicates that each administration group showed no significant effect on

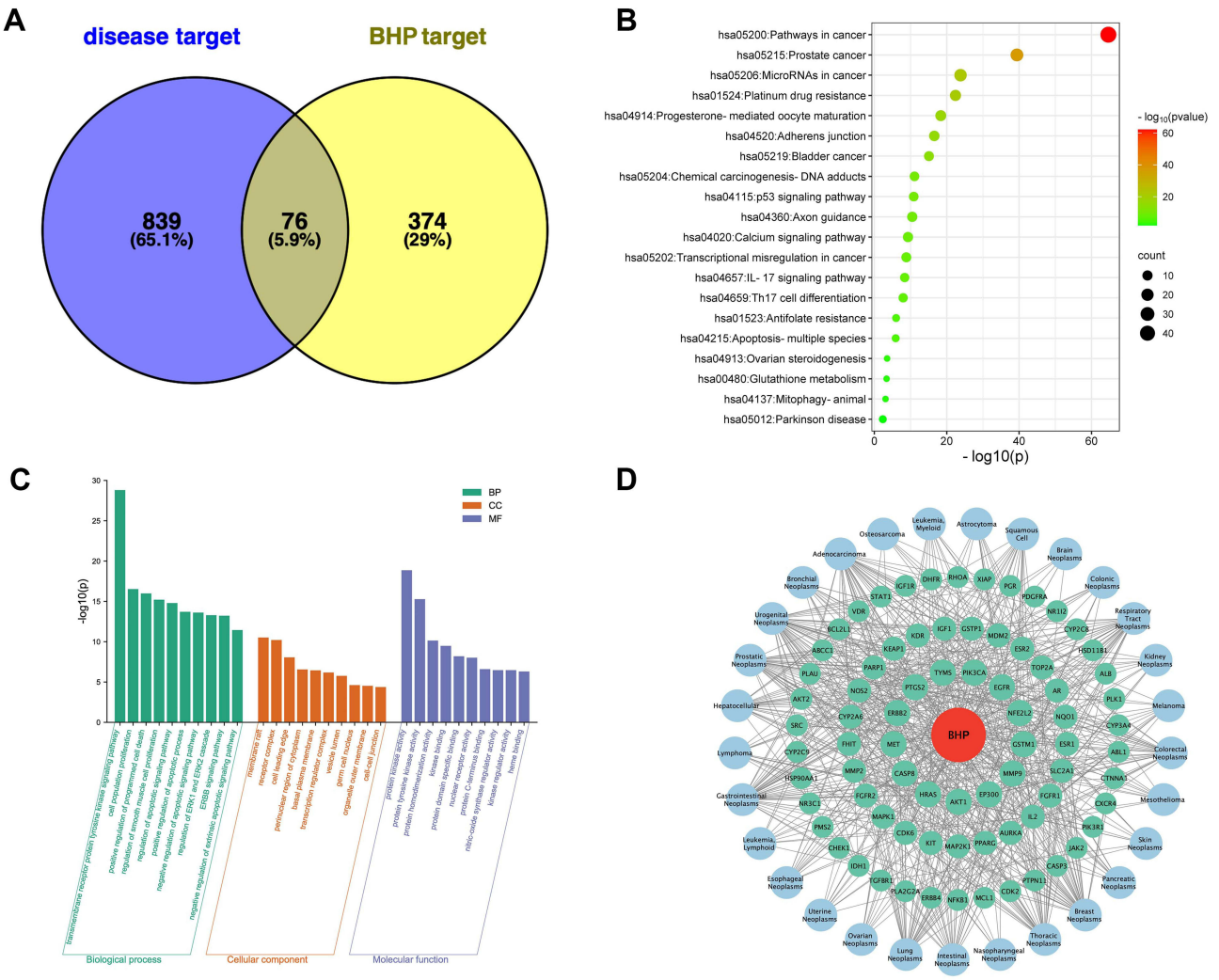

Figure 8 (**A**) Venn diagram of disease targets and BHP inverse prediction targets. (**B**) KEGG pathway analysis and GO enrichment analysis (**C**) of core targets. (**D**) BHP-target-tumor network. Red represents BHP; green represents target; blue represents tumor-related disease.

the body weight of the mice. Thus, the administrated group showed good biocompatibility and no evident toxicity in mice. Tumors treated with control saline and BHP proliferated and exhibited typical growth behaviors. In contrast, tumor growth was significantly inhibited after the injection of NV and BHP-NV (Figure 9C). Tumor growth was significantly inhibited when the isolated tumor tissue was weighed after treatment (Figure 9D). As expected, all results indicated that the BHP-NV group performed better than the other groups over three weeks.

Hematoxylin and eosin (H&E) staining was performed to observe the morphology of the tumor cells and assess antitumor efficiency (Figure 9E). Most tumor cells in the saline and free BHP groups exhibited normal morphology. In contrast, tumor cells in the BHP-NV group showed evident apoptotic morphology, including nuclear shrinkage. This finding was consistent with the results of TUNEL staining (Figure 9E). The highest intensity of green fluorescence was observed in the BHP-NV group. This indicates that significant cell apoptosis occurred after administration. These results illustrate that, owing to RPPMMRA, BHP is delivered by NVs into tumor cells to induce cell apoptosis and inhibit tumor growth. H&E staining was performed on major organs, including the heart, liver, spleen, lungs, and kidneys (Figure 10). Neither histopathological abnormalities nor damage was evident after intravenous injection, suggesting that BHP-NV is a safe drug delivery system in vivo.

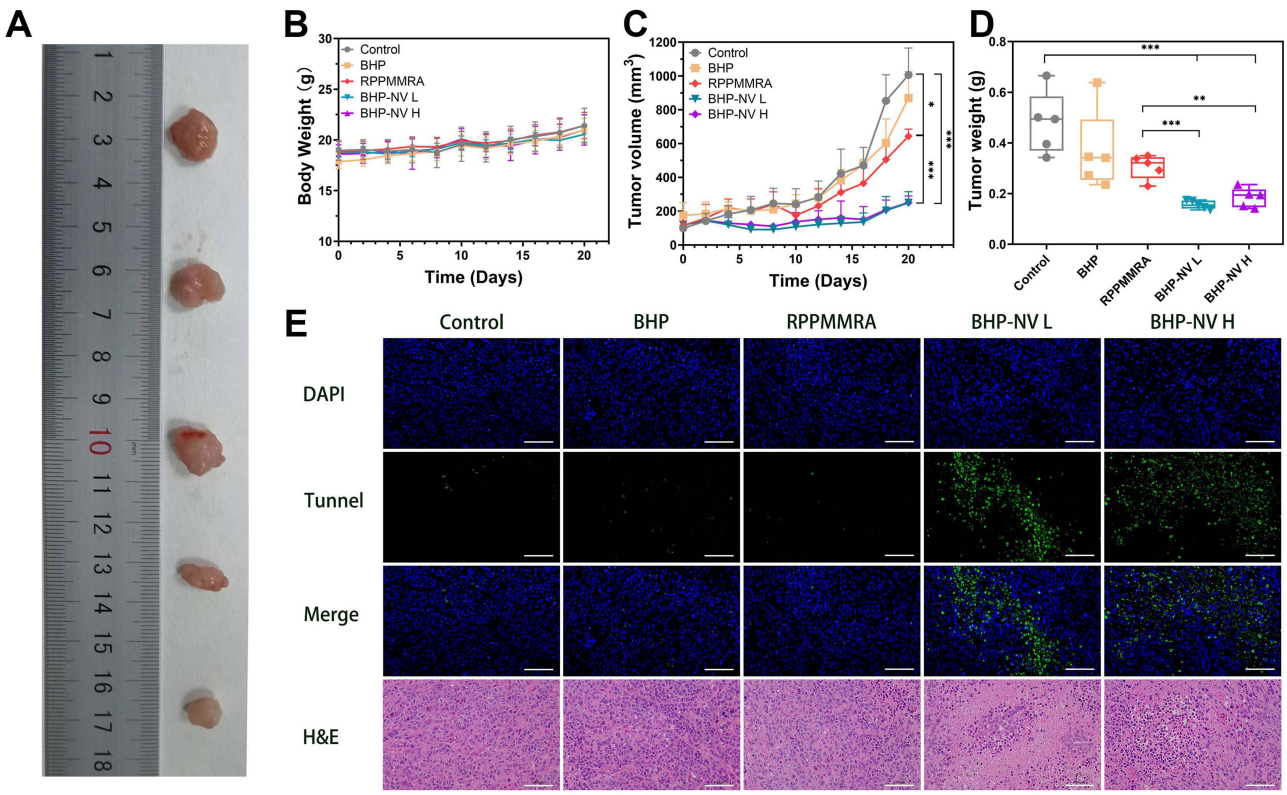

Figure 9 In Vivo tumor inhibition performance (**A**) Photograph of tumor tissues from mice treated with saline, BHP, RPPMMRA, BHP-NV L, and BHP-NV H at the end of the study. (**B**) Real-time observation of body weight in vivo after treatment with samples. (**C**) Real-time observation of tumor sizes in vivo after treatment with samples. (**D**) Weight of tumor tissue after treatment. (**E**) TUNEL and H&E staining of tumor tissue after treatment. Significant differences are presented as *, **, and ***, indicating $p < 0.05$, $p < 0.01$, and $p < 0.001$, respectively.

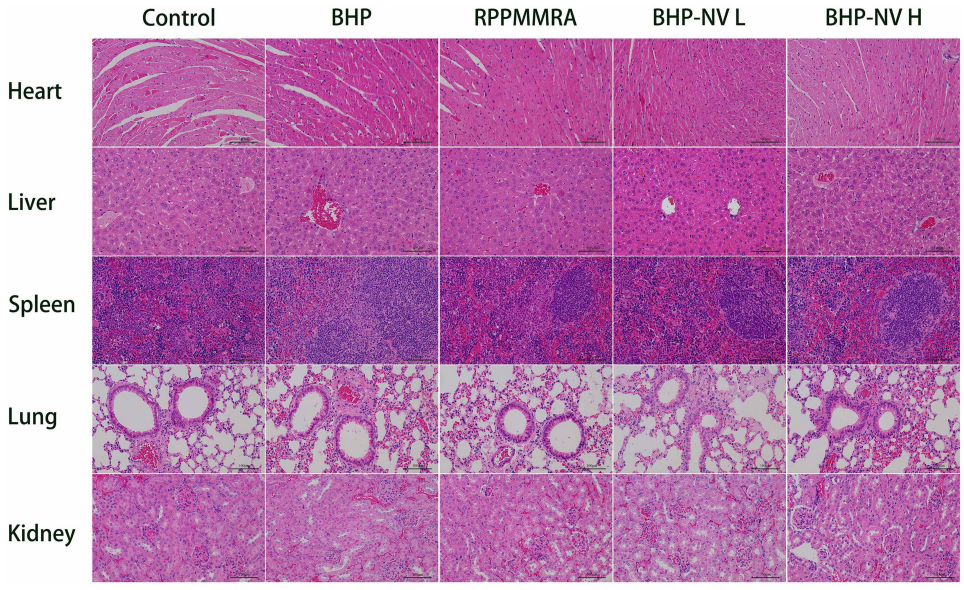

Figure 10 H&E staining of major organs (heart, liver, spleen, lungs, and kidneys) after treatment.

Conclusion

A short peptide, BHP, with 20 amino acids, based on the Bax-BH3 domain, was constructed and modified using a fluorescent drug vector. The results indicated that NV had good biocompatibility and low toxicity and could be used to deliver anticancer drugs. BHP-NV was efficiently internalized into A549 cells in 6 h with a drug loading capacity of 15.2% and was of appropriate size, resulting in a cell survival rate lower than 50.0% at 75 μg/mL. Flow cytometry and other experiments established that BHP significantly promotes apoptosis. Colony experiments demonstrated that BHP inhibited the proliferation of cancer cells. BHP-NV showed a significant pro-apoptotic effect, which may provide a novel approach for understanding the structure and function of BH3 and for the selection of pro-apoptotic peptides. The potential therapeutic effects of BHP were evaluated by reverse molecular docking. BHP peptides can regulate apoptosis, indicating their pleiotropic cancer treatment prospects. Furthermore, in vivo experiments established that BHP-NV has excellent tumor targeting and inhibition functions in tumor-bearing mice. Drug tracing and imaging can be performed simultaneously in the future diagnosis and treatment of diseases by synthesizing the fluorescence properties of the nanovector, thereby realizing the integration of disease diagnosis and disease detection visualization.

Author Contributions

All authors made a significant contribution to the work reported, whether that is in the conception, study design, execution, acquisition of data, analysis and interpretation, or in all these areas; took part in drafting, revising or critically reviewing the article; gave final approval of the version to be published; have agreed on the journal to which the article has been submitted; and agree to be accountable for all aspects of the work.

Funding

This work was supported by grants from the National Natural Science Foundation of China [82172100] and the Project of Science and Technology Department of Jilin Province, China [No. 20210402039GH, 20220101299JC].

Disclosure

The authors declare that they have no known competing financial interests or personal relationships that could have appeared to influence the work reported in this paper.

References

1. Min KA, Maharjan P, Ham S, Shin MC. Pro-apoptotic peptides-based cancer therapies: challenges and strategies to enhance therapeutic efficacy. *Arch Pharm Res*. 2018;41(6):594–616. doi:10.1007/s12272-018-1038-y
2. Kuwana T, Bouchier-Hayes L, Chipuk JE, et al. BH3 domains of BH3-only proteins differentially regulate Bax-mediated mitochondrial membrane permeabilization both directly and indirectly. *Mol Cell*. 2005;17(4):525–535. doi:10.1016/j.molcel.2005.02.003
3. Rodik RV, Cherenok SO, Postupalenko VY, et al. Anionic amphiphilic calixarenes for peptide assembly and delivery. *J Colloid Interface Sci*. 2022;624:270–278. doi:10.1016/j.jcis.2022.05.124
4. Yang B, Liu D, Huang Z. Synthesis and helical structure of lactam bridged BH3 peptides derived from pro-apoptotic Bcl-2 family proteins. *Bioorg Med Chem Lett*. 2004;14(6):1403–1406. doi:10.1016/j.bmcl.2003.09.101
5. Lohner K, Hilpert K. Antimicrobial peptides: cell membrane and microbial surface interactions. *Biochim Biophys Acta*. 2016;1858(5):915–917. doi:10.1016/j.bbamem.2016.03.005
6. Gomes B, Augusto MT, Felicio MR, et al. Designing improved active peptides for therapeutic approaches against infectious diseases. *Biotechnol Adv*. 2018;36(2):415–429. doi:10.1016/j.biotechadv.2018.01.004
7. Raucher D, Moktan S, Massodi I, Bidwell GL. Therapeutic peptides for cancer therapy. Part II - cell cycle inhibitory peptides and apoptosis-inducing peptides. *Expert Opin Drug Deliv*. 2009;6(10):1049–1064. doi:10.1517/17425240903158909
8. Wu D, Gao Y, Qi Y, Chen L, Ma Y, Li Y. Peptide-based cancer therapy: opportunity and challenge. *Cancer Lett*. 2014;351(1):13–22. doi:10.1016/j.canlet.2014.05.002
9. Albericio F, Kruger HG. Therapeutic peptides FOREWORD. *Future Med Chem*. 2012;4(12):1527–1531. doi:10.4155/FMC.12.94
10. Thundimadathil J. Cancer treatment using peptides: current therapies and future prospects. *J Amino Acids*. 2012;2012:967347. doi:10.1155/2012/967347
11. Walensky LD, Bird GH. Hydrocarbon-stapled peptides: principles, practice, and progress. *J Med Chem*. 2014;57(15):6275–6288. doi:10.1021/jm4011675
12. Czabotar PE, Lessene G, Strasser A, Adams JM. Control of apoptosis by the BCL-2 protein family: implications for physiology and therapy. *Nat Rev Mol Cell Biol*. 2013;15(1):49–63. doi:10.1038/nrm3722
13. Cory S, Roberts AW, Colman PM, Adams JM. Targeting BCL-2-like proteins to kill cancer cells. *Trends Cancer*. 2016;2(8):443–460. doi:10.1016/j.trecan.2016.07.001

14. Kvansakul M, Hinds MG. The Bcl-2 family: structures, interactions and targets for drug discovery. *Apoptosis*. 2015;20(2):136–150. doi:10.1007/s10495-014-1051-7
15. Martinou JC, Youle RJ. Mitochondria in apoptosis: bcl-2 family members and mitochondrial dynamics. *Dev Cell*. 2011;21(1):92–101. doi:10.1016/j.devcel.2011.06.017
16. Czabotar PE, Westphal D, Dewson G, et al. Bax crystal structures reveal how BH3 domains activate Bax and nucleate its oligomerization to induce apoptosis. *Cell*. 2013;152(3):519–531. doi:10.1016/j.cell.2012.12.031
17. Chen R, Braun GB, Luo X, Sugahara KN, Teesalu T, Ruoslahti E. Application of a proapoptotic peptide to intratumorally spreading cancer therapy. *Cancer Res*. 2013;73(4):1352–1361. doi:10.1158/0008-5472.CAN-12-1979
18. Zhang X, Yan Q, Wang J, Xu L, Guo Y. The antitumor activity of Bax BH3 peptide delivered by gold nanoparticles. *Front Mater*. 2023;9. doi:10.3389/fmats.2022.1099997
19. Chytil P, Koziolova E, Etrych T, Ulbrich K. HPMA copolymer-drug conjugates with controlled tumor-specific drug release. *Macromol Biosci*. 2018;18(1). doi:10.1002/mabi.201700209
20. Geyik C, Ciftci M, Demir B, et al. Controlled release of anticancer drug Paclitaxel using nano-structured amphiphilic star-hyperbranched block copolymers. *Polym Chem*. 2015;6(30):5470–5477. doi:10.1039/c5py00780a
21. Liu SY, Lo SN, Lee WC, Hsu WC, Lee TW, Chang CH. Evaluation of nanotargeted (111)in-cyclic RGDfK-liposome in a human melanoma xenotransplantation model. *Int J Mol Sci*. 2021;22(3):1.
22. Bhosale RR, Gangadharappa HV, Osmani RAM, Gowda DV. Design and development of polymethylmethacrylate-grafted gellan gum (PMMA-g-GG)-based pH-sensitive novel drug delivery system for antidiabetic therapy. *Drug Deliv Transl Res*. 2020;10(4):1002–1018. doi:10.1007/s13346-020-00776-7
23. Xie N, Feng K, Chen B, et al. A modular designed copolymer with anti-thrombotic activity and imaging capability. *Chem Commun*. 2014;50(67):9539–9542. doi:10.1039/c4cc04649h
24. Dalela M, Shrivastav TG, Kharbanda S, Singh H. pH-sensitive biocompatible nanoparticles of paclitaxel-conjugated poly(styrene-co-maleic acid) for anticancer drug delivery in solid tumors of syngeneic mice. *ACS Appl Mater Interfaces*. 2015;7(48):26530–26548. doi:10.1021/acsami.5b07764
25. Ma M, Gao N, Sun Y, Ren J, Qu X. A near-infrared responsive drug sequential release system for better eradicating amyloid aggregates. *Small*. 2017;13(46). doi:10.1002/smll.201701817
26. Rondon EP, Benabdoun HA, Vallieres F, et al. Evidence supporting the safety of pegylated diethylaminoethyl-chitosan polymer as a nanovector for gene therapy applications. *Int J Nanomedicine*. 2020;15:6183–6200. doi:10.2147/IJN.S252397
27. Ma FH, An Y, Wang J, Song Y, Liu Y, Shi L. Synthetic nanochaperones facilitate refolding of denatured proteins. *ACS Nano*. 2017;11(10):10549–10557. doi:10.1021/acsnano.7b05947
28. Chytil P, Kostka L, Etrych T. HPMA Copolymer-Based Nanomedicines in Controlled Drug Delivery. *J Pers Med*. 2021;11(2). doi:10.3390/jpm11020115
29. Saeedi T, Alotaibi HF, Prokopovich P. Polymer colloids as drug delivery systems for the treatment of arthritis. *Adv Colloid Interface Sci*. 2020;285:102273. doi:10.1016/j.cis.2020.102273
30. Hu F, Wang H, Zhang S, et al. Inhibition of myeloid differentiation factor 88 signaling mediated by histidine-grafted poly(beta-amino ester) ester nanovector induces donor-specific liver allograft tolerance. *Int J Nanomedicine*. 2015;10:4367–4382. doi:10.2147/IJN.S81413
31. Cui H, Zhang M, Zhang L, et al. pH-responsive organic/inorganic hybrid nanocolloids for transcellular delivery of ribonucleolytic payloads toward targeted anti-glioma therapy. *J Colloid Interface Sci*. 2023;634:388–401. doi:10.1016/j.jcis.2022.12.018
32. Lammers T, Peschke P, Kuhnlein R, et al. Effect of radiotherapy and hyperthermia on the tumor accumulation of HPMA copolymer-based drug delivery systems. *J Control Release*. 2007;117(3):333–341. doi:10.1016/j.jconrel.2006.10.032
33. Zhang R, Luo K, Yang J, et al. Synthesis and evaluation of a backbone biodegradable multiblock HPMA copolymer nanocarrier for the systemic delivery of paclitaxel. *J Control Release*. 2013;166(1):66–74. doi:10.1016/j.jconrel.2012.12.009
34. Subasic CN, Ardana A, Chan LJ, et al. Poly(HPMA-co-NIPAM) copolymer as an alternative to polyethylene glycol-based pharmacokinetic modulation of therapeutic proteins. *Int J Pharm*. 2021;608:121075. doi:10.1016/j.ijpharm.2021.121075
35. Wang F, Li L, Sun W, et al. A novel alpha(V)beta(3) ligand-modified HPMA copolymers for anticancer drug delivery. *J Drug Target*. 2018;26(3):231–241. doi:10.1080/1061186X.2017.1365872
36. Yuan JC, Xie XL, Zeng XW, Guo HY, Miao CP. Tumor targeting of HPMA copolymer conjugates containing sulfadiazine groups. *Chin Chem Lett*. 2012;23(7):875–878. doi:10.1016/j.cclet.2012.05.005
37. Luo Y, Bernshaw NJ, Lu ZR, Kopecek J, Prestwich GD. Targeted delivery of doxorubicin by HPMA copolymer-hyaluronan bioconjugates. *Pharm Res*. 2002;19(4):396–402. doi:10.1023/A:1015170907274
38. Lin W, Klein J. Control of surface forces through hydrated boundary layers. *Curr Opin Colloid Interface Sci*. 2019;44:94–106. doi:10.1016/j.cocis.2019.10.001
39. Borgman MP, Coleman T, Kolhatkar RB, Geyser-Stoops S, Line BR, Ghandehari H. Tumor-targeted HPMA copolymer-(RGDfK)-(CHX-A"-DTPA) conjugates show increased kidney accumulation. *J Control Release*. 2008;132(3):193–199. doi:10.1016/j.jconrel.2008.07.014
40. Journo-Gershfeld G, Kapp D, Shamay Y, Kopecek J, David A. Hyaluronan oligomers-HPMA copolymer conjugates for targeting paclitaxel to CD44-overexpressing ovarian carcinoma. *Pharm Res*. 2012;29(4):1121–1133. doi:10.1007/s11095-012-0672-1
41. Onishi Y, Eshita Y, Ji RC, et al. Anticancer efficacy of a supramolecular complex of a 2-diethylaminoethyl-dextran-MMA graft copolymer and paclitaxel used as an artificial enzyme. *Beilstein J Nanotechnol*. 2014;5:2293–2307. doi:10.3762/bjnano.5.238
42. Maeda H. Toward a full understanding of the EPR effect in primary and metastatic tumors as well as issues related to its heterogeneity. *Adv Drug Deliv Rev*. 2015;91:3–6. doi:10.1016/j.addr.2015.01.002
43. Echigo H, Mishiro K, Fuchigami T, Shiba K, Kinuya S, Ogawa K. Synthesis and evaluation of a dimeric RGD peptide as a preliminary study for radiotheranostics with radiohalogens. *Molecules*. 2021;26(20). doi:10.3390/molecules26206107
44. Garanti T, Alhnan MA, Wan KW. RGD-decorated solid lipid nanoparticles enhance tumor targeting, penetration and anticancer effect of asiatic acid. *Nanomedicine*. 2020;15(16):1567–1583. doi:10.2217/nnm-2020-0035
45. Zhang J, Su X, Weng L, et al. Gadolinium-hybridized mesoporous organosilica nanoparticles with high magnetic resonance imaging performance for targeted drug delivery. *J Colloid Interface Sci*. 2023;633:102–112. doi:10.1016/j.jcis.2022.11.085

46. Zhang J, Yuan ZF, Wang Y, et al. Multifunctional envelope-type mesoporous silica nanoparticles for tumor-triggered targeting drug delivery. *J Am Chem Soc*. 2013;135(13):5068–5073. doi:10.1021/ja312004m
47. Li C, Wang W, Xi Y, et al. Design, preparation and characterization of cyclic RGDfK peptide modified poly(ethylene glycol)-block-poly(lactic acid) micelle for targeted delivery. *Mater Sci Eng C Mater Biol Appl*. 2016;64:303–309. doi:10.1016/j.msec.2016.03.062
48. Li L, Chen X, Yu J, Yuan S. Preliminary clinical application of RGD-containing peptides as PET radiotracers for imaging tumors. *Front Oncol*. 2022;12:837952. doi:10.3389/fonc.2022.837952
49. Jiang Z, Yuan B, Qiu N, et al. Manganese-zeolitic imidazolate frameworks-90 with high blood circulation stability for MRI-guided tumor therapy. *Nanomicro Lett*. 2019;11(1):61. doi:10.1007/s40820-019-0292-y
50. Wang ZY, Li ZY, Sun ZL, et al. Visualization nanozyme based on tumor microenvironment "unlocking" for intensive combination therapy of breast cancer. *Sci Adv*. 2020;6(48):eabc8733. doi:10.1126/sciadv.abc8733
51. Zhou J, Li K, Qin H, et al. Programmed-stimuli responsive carrier-free multidrug delivery system for highly efficient trimodal combination therapy. *J Colloid Interface Sci*. 2023;637:453–464. doi:10.1016/j.jcis.2023.01.091
52. Reichel D, Sagong B, Teh J, et al. Near infrared fluorescent nanoplatform for targeted intraoperative resection and chemotherapeutic treatment of glioblastoma. *ACS Nano*. 2020;14(7):8392–8408. doi:10.1021/acsnano.0c02509
53. Zhu WB, Liang JK, Tan JY, et al. Real-time visualization and quantification of oncolytic M1 virus in vitro and in vivo. *Hum Gene Ther*. 2021;32(3–4):158–165. doi:10.1089/hum.2020.273
54. Wu B, Li K, Sun F, et al. Trifunctional graphene quantum Dot@LDH integrated nanoprobes for visualization therapy of gastric cancer. *Adv Healthc Mater*. 2021;10(16):e2100512. doi:10.1002/adhm.202100512
55. Yu L, Zhang JF, Li M, et al. Combining viscosity-restricted intramolecular motion and mitochondrial targeting leads to selective tumor visualization. *Chem Commun*. 2020;56(49):6684–6687. doi:10.1039/d0cc02943b
56. Wang X, Ramamurthy G, Shirke AA, et al. Photodynamic therapy is an effective adjuvant therapy for image-guided surgery in prostate cancer. *Cancer Res*. 2020;80(2):156–162. doi:10.1158/0008-5472.CAN-19-0201
57. Colby AH, Berry SM, Moran AM, et al. Highly specific and sensitive fluorescent nanoprobes for image-guided resection of sub-millimeter peritoneal tumors. *ACS Nano*. 2017;11(2):1466–1477. doi:10.1021/acsnano.6b06777
58. Luo S, Jiang T, Long L, et al. A dual PMMA/calcium sulfate carrier of vancomycin is more effective than PMMA-vancomycin at inhibiting Staphylococcus aureus growth in vitro. *FEBS Open Bio*. 2020;10(4):552–560. doi:10.1002/2211-5463.12809
59. Prabakaran S, Jeyaraj M, Nagaraj A, Sadasivuni KK, Rajan M. Polymethyl methacrylate–ovalbumin @ graphene oxide drug carrier system for high anti-proliferative cancer drug delivery. *Appl Nanosci*. 2019;9(7):1487–1500. doi:10.1007/s13204-019-00950-5
60. Lu CY, Church DC, Learn GD, Pokorski JK, von Recum HA. Modified cyclodextrin microparticles to improve PMMA drug delivery without mechanical loss. *Macromol Biosci*. 2021;21(7):e2000328. doi:10.1002/mabi.202000328
61. Scherf R, Müller LS, Grosch D, Hübner EG, Oppermann W. Investigation on the homogeneity of PMMA gels synthesized via RAFT polymerization. *Polymer*. 2015;58:36–42. doi:10.1016/j.polymer.2014.12.035
62. Zhang L, Su F, Buizer S, et al. A polymer-based ratiometric intracellular glucose sensor. *Chem Commun*. 2014;50(52):6920–6922. doi:10.1039/c4cc01110d
63. Zhang L, Su F, Buizer S, et al. A dual sensor for real-time monitoring of glucose and oxygen. *Biomaterials*. 2013;34(38):9779–9788. doi:10.1016/j.biomaterials.2013.09.031
64. Lv Y, Ding G, Zhai J, Guo Y, Nie G, Xu L. A superparamagnetic Fe3O4-loaded polymeric nanocarrier for targeted delivery of evodiamine with enhanced antitumor efficacy. *Colloids Surf B Biointerfaces*. 2013;110:411–418. doi:10.1016/j.colsurfb.2013.04.038
65. Mitsukami Y, Donovan MS, Lowe AB, McCormick CL. Water-soluble polymers. 81. Direct synthesis of hydrophilic styrenic-based homopolymers and block copolymers in aqueous solution via RAFT. *Macromolecules*. 2001;34(7):2248–2256. doi:10.1021/ma0018087
66. Anžlovar A, Huskić M, Žagar E. Modification of nanocrystalline cellulose for application as a reinforcing nanofiller in PMMA composites. *Cellulose*. 2015;23(1):505–518. doi:10.1007/s10570-015-0786-9
67. Barsbay M, Güven O, Davis TP, Barner-Kowollik C, Barner L. RAFT-mediated polymerization and grafting of sodium 4-styrenesulfonate from cellulose initiated via γ-radiation. *Polymer*. 2009;50(4):973–982. doi:10.1016/j.polymer.2008.12.027
68. Utama RH, Jiang Y, Zetterlund PB, Stenzel MH. Biocompatible glycopolymer nanocapsules via inverse miniemulsion periphery RAFT polymerization for the delivery of gemcitabine. *Biomacromolecules*. 2015;16(7):2144–2156. doi:10.1021/acs.biomac.5b00545
69. Liu X, Ouyang S, Yu B, et al. PharmMapper server: a web server for potential drug target identification using pharmacophore mapping approach. *Nucleic Acids Res*. 2010;38(Web Server issue):W609–14. doi:10.1093/nar/gkq300
70. Wang X, Pan C, Gong J, Liu X, Li H. Enhancing the enrichment of pharmacophore-based target prediction for the polypharmacological profiles of drugs. *J Chem Inf Model*. 2016;56(6):1175–1183. doi:10.1021/acs.jcim.5b00690
71. Wang X, Shen Y, Wang S, et al. PharmMapper 2017 update: a web server for potential drug target identification with a comprehensive target pharmacophore database. *Nucleic Acids Res*. 2017;45(W1):W356–W360. doi:10.1093/nar/gkx374
72. Zhou Y, Zhou B, Pache L, et al. Metascape provides a biologist-oriented resource for the analysis of systems-level datasets. *Nat Commun*. 2019;10(1):1523. doi:10.1038/s41467-019-09234-6
73. Khalilov R. A comprehensive review of advanced nano-biomaterials in regenerative medicine and drug delivery. *Adv Biol Earth Sci*. 2023;8(1):5–18.
74. Eftekhari A, Kryschi C, Pamies D, et al. Natural and synthetic nanovectors for cancer therapy. *Nanotheranostics*. 2023;7(3):236–257. doi:10.7150/ntno.77564
75. Ipek P, Baran MF, Baran A, et al. Green synthesis and evaluation of antipathogenic, antioxidant, and anticholinesterase activities of gold nanoparticles (Au NPs) from Allium cepa L. peel aqueous extract. *Biomass Convers Biorefin*. 2023;31:1. doi:10.1007/s13399-023-04362-y